Journal of Geophysical Research: Solid Earth

RESEARCH ARTICLE
10.1029/2018JB015498

Mapping the Basement of the Ebro Basin in Spain With Seismic Ambient Noise Autocorrelations

Paula Romero[1] **and Martin Schimmel**[1]

[1] Institute of Earth Sciences Jaume Almera-CSIC, Barcelona, Spain

Key Points:
- We estimate the high-frequency reflection response for stations in the Ebro Basin with phase autocorrelations of ambient seismic noise
- The study includes the analysis of time variability and frequency stability of reflections and elimination of ambiguities adding well data
- Final result is a comprehensive map of the Paleozoic basement in the Ebro Basin, Spain

Supporting Information:
- Supporting Information S1

Correspondence to:
P. Romero,
paularomerolopes@gmail.com

Citation:
Romero, P., & Schimmel, M. (2018). Mapping the basement of the Ebro Basin in Spain with seismic ambient noise autocorrelations. *Journal of Geophysical Research: Solid Earth*, *123*, 5052–5067. https://doi.org/10.1029/2018JB015498

Received 15 JAN 2018
Accepted 14 MAY 2018
Accepted article online 19 MAY 2018
Published online 16 JUN 2018

Abstract Single-station autocorrelations of seismic ambient noise allow to obtain the shallow subsurface reflection response without the need of any active source or earthquake. Recently, crustal-scale studies successfully applied this method to map the crust-mantle boundary. These studies employed different processing methodologies to stabilize and identify the weak-amplitude reflections. Here we also analyze noise autocorrelations but use higher-frequency bands to map the basement of the Ebro Basin in Spain. This basin has a nonuniform basement structure due to its complex evolution. We tested two autocorrelation methods (the classical and phase cross correlation) to retrieve the *P* wave reflection response for seismic broadband stations located in the basin. The phase correlation approach is amplitude unbiased since based on the instantaneous phase coherence of analytic signals. It is insensitive to the background seismicity from the Pyrenees and other noise and proved to be the more efficient approach to retrieve *P* wave reflections from the Paleozoic basement. The detected signals per station are quite stable and show only a small time variability. We also show that sidelobes caused by the convolution of a delta pulse at zero time lag with the effective noise source time function do not affect our measurements and compare the measured noise autocorrelations with synthetic data for lithological profiles from neighboring wells. The a priori information from well data was essential to identify the signals and to finally map the discontinuity in between and beyond the well positions. Our final result is a comprehensive map of the Paleozoic basement in the Ebro Basin.

Plain Language Summary The autocorrelation, correlating a signal with itself, of ambient seismic noise permits to achieve an approximation of the zero-offset reflection response of the structure beneath a seismic station. With this approach no active source or earthquake is needed and few days of continuous noise recordings are usually sufficient to identify reflections of discontinuities at crustal scale. Autocorrelations of ambient noise have already been successfully applied to retrieve *P* wave reflections for crustal scale imaging. In this article, we also use ambient noise autocorrelations but use higher-frequency bands with the main objective to resolve and map the Paleozoic basement of the Ebro Basin in North Spain. For this purpose we tested two different autocorrelation methods. Both methods, the classical approach and the phase cross-correlation, are based on independent strategies. We finally use the phase cross-correlation approach since it does not depend on signal amplitude information and since it proved to be the more efficient approach to retrieve the small-amplitude reflections from the basement. We further analyzed the time and frequency stability of these signals and used information from neighboring well logs to reduce ambiguities in the data interpretation. The well data were essential to correctly identify the signals and to finally map the Paleozoic basement in between and beyond the well positions. At the end, we discuss the new Ebro Basin map and the performance of our approaches.

1. Introduction

Conventional seismic interferometry is based on cross-correlating wave fields recorded at two seismic stations to construct the Green's Function between both receivers, that is, to obtain the impulse response at one receiver as if the second one is a virtual source. When the distance between the two receivers is decreased to zero, then the cross-correlation function becomes an autocorrelation and provides a zero-offset Green's function, which contains information of the local structure beneath the seismic station. This principle goes back to Claerbout (1968) who first showed that for an one-dimensional (1-D) media, the reflection response can be recovered by the autocorrelation of a transmitted plane wave originated in the subsurface, including the body wave primary reflections and their multiples. Wapenaar (2004) extended Claerbout's findings to

two-dimensional (2-D) and three-dimensional (3-D) acoustic and elastic media. In practice, the exact Green's function is unknown and likely not fully reconstructed due to wave fields which are not diffuse and we therefore refer to the empirical Green's function (EGF).

Autocorrelation and cross correlation of ambient noise have been applied to dense station deployments to retrieve *P* wave reflections for crustal-scale imaging (e.g., Ruigrok et al., 2011, 2012). With larger interstation distances only autocorrelations can be used to retrieve zero-offset Moho reflections as shown by Tibuleac and von Seggern (2012). They closely follow the ambient noise processing flow described by Bensen et al. (2007) to map the crust-mantle boundary (Moho) topography in Nevada, United States. Also in Nevada, Oren and Nowack (2016) tested a different processing strategy with spectral whitening and different frequency band filters and compared their results with those obtained in a different tectonic setting in the central United States. Follow-up studies often use modified processing approaches to improve or stabilize the reflection response, due to the usually encountered variability and multitude of signals, which hampers the identification of reflections. For instance, Gorbatov et al. (2013) advocate a regularized spectral division instead of a plain autocorrelogram computation to mitigate the effect of the source excitation, which they use to detect Moho reflections in Australia. Kennett et al. (2015) further extended this work using spatial autocorrelogram stacks for neighboring stations to enhance the coherent portion of the crustal reflectivity. They also show the importance of existing Moho models to help the signal identification and to finally determine improved Moho depth estimates. The regularized spectral division approach has also been employed by Saygin et al. (2017) together with the phase-weighted stack (Schimmel & Paulssen, 1997) to map the Jakarta Basin structure. In contrast to these studies, Taylor et al. (2016) map the North Anatolian crust and fault zone using the phase cross correlation (PCC) by Schimmel (1999) to ensure that the coherent *P* wave reflections are retrieved independently of amplitude. Phase-incoherent signals are attenuated by this approach, which help the signal detection and identification. All the different noise autocorrelation studies successfully mapped their target reflectors and are now catching increasing attention since the approach is on the way to become an alternative to the classical receiver functions (Galetti & Curtis, 2012; Langston, 1979, among others).

The first recent comprehensive map of the Paleozoic basement in the Ebro Basin was published in 1990 based on sparse well data and low-quality seismic profiles in addition to geological surface observations (Instituto Tecnológico y Geominero de España - ITGE, 1990). In 2010, an updated version of the map was published in the context of CO_2 storage studies in Spain (Instituto Geológico y Minero de España - IGME, 2009). This map was built with the same geophysical data from 1990 but adding surface information from geological cross sections mainly in the borders of the basin. In this paper, our main goals are to build (and present) a new map of the Ebro Basin Paleozoic basement determined from new seismic data and approaches and to analyze the appropriateness and performance of the ambient noise autocorrelations for this purpose. The approach enables a fast and consistent imaging of the basement structure and is much cheaper than active seismic surveys or drilling wells. The shallow reflector depths, however, demand to work in frequency bands that are higher (about 3–18 Hz) than the frequencies usually employed to map the Moho discontinuity (about 0.5–2 Hz). The extension to high frequencies, structural complexities, and local seismicity may hamper (or limit) the applicability of the method. Here we show that we can take advantage of the instantaneous phase coherence concept of the PCC to detect the weak-amplitude reflections for 42 seismic stations in the Ebro Basin, which we then use together with well data to build a more accurate basin map.

Besides our prime motivation, knowledge of basin geometry is an important constraint for studies on basin evolution and corresponding geodynamics and tectonic evolution of the region. For instance, flexural isostasy, erosion with climate and fluvial transport, and tectonic deformation of surrounding cordilleras are processes that control the basin evolution. Accurate basin maps therefore help, through the geometry and mass budget, to advance our understanding on related surface processes and their causes (e.g., Garcia-Castellanos et al., 2003). Besides, studies related to the tectonic evolution, the accurate knowledge of basin structure is also important for seismic site response or amplification studies, which are of major seismological and engineering interest. The 3-D basin structure can lead through diffraction and scattering inside the basin and/or through basin-edge generated surface waves to an increased amplitude and duration of ground shaking (e.g., Feng & Ritzwoller, 2017; Gil-Zepeda et al., 2002; Narayan et al., 2016). The wave propagation in the basin can be very complex, and 3-D numerical approaches are required to understand the local ground amplification.

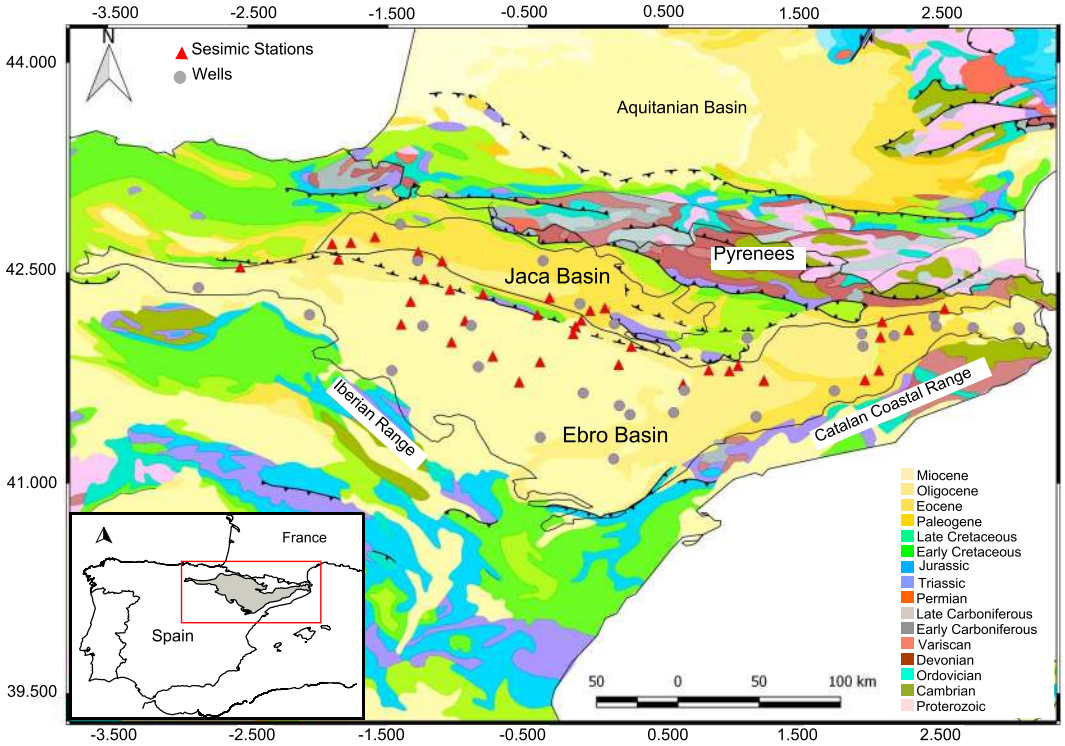

Figure 1. Geological map of the Ebro Basin with the seismic stations (red triangles) and well locations (gray circles) used in this study. Data source: One Geology Project (http://www.onegeology.org/ and IGME—Geological Map of Spain 1/1.000.000).

1.1. Geological Context

During the Mesozoic (252–66 Ma), the Iberian Plate was subjected to an extensional regime related to the opening of the Atlantic, the Tethys Ocean, and the Bay of Biscay, which developed the Iberian Rift System. In the area that is now located near the Ebro Basin and its adjacent mountain ranges, an intracratonic basin was formed over the Variscan basement accumulating continental and shallow marine sediments from Permian to Late Mesozoic times (Verges et al., 2002). The so called Iberian Basin comprised an asymmetrical half-graben system bounded by NW-SE lystric faults and a depocenter, which migrated steadily to the northeast with time (Arche & López-Gómez, 1996).

However, in the Late Cretaceous, the north-south convergence of Africa and Eurasia (Alpine Orogen) produced the first inversions of the rather stable Mesozoic Iberian Basin following the crustal weakness related to the extensional faults of the Iberian Rift System. In this context, the Pyrenees Mountain Range was formed and, as a consequence, started the development of the foreland Cenozoic Ebro Basin (Gaspar et al., 2001). In Early Cretaceous, the uplift of the southern part of the basin caused partial erosion of Mesozoic sediments. The adjacent Iberian Range and Catalan Coastal Range were also formed in the interior of the Iberian plate in response to this compressive movement and are now the modern limits of the Ebro Basin. In Late Oligocene the development of these mountain ranges closed the basin, which was, then, submitted to intense erosion. The continuous development of the thrust system allowed the uplift of the External Sierra (southern Pyrenees) during the Eocene isolating Sub-Pyrenees basins (e.g., Jaca Basin) from the foreland Ebro Basin. The isolated Jaca Basin received a different sediment load, mainly detritic from the adjacent Pyrenees (Hogan & Burbank, 1996). The final deformation stage occurred in Early Miocene leading to the present configuration (Figure 1).

The crystalline basement of the Ebro Basin comprised Paleozoic rocks from the Variscan Orogen and dips toward north submerging under the first marginal ridges of the Pyrenees system. Overlying it are the eroded Mesozoic sequence and the Cenozoic sediments with low tectonic expressions. In the Sub-Pyrenees (Jaca Basin) it is possible to follow the Paleozoic basement dipping north with a lower angle (Lanaja, 1987). On the other hand, the complex evolution of the Ebro Basin as a foreland basin generated a nonuniform Cenozoic

basement structure. It dips mainly northward in the central and east part of the basin and northwest in the west limit. The rocks underlying the Cenozoic Ebro basin are aged Paleozoic and Permo-Triassic in the east, Jurassic in the center, and Permo-Triassic to the west of the basin with Cretaceous rocks sparsely found (Gaspar et al., 2001).

1.2. Methods

Retrieving the Earth's reflection response at one station by seismic interferometry involves three basic steps: preprocessing the recorded ambient noise, autocorrelation of the preprocessed data, and stacking of the autocorrelation functions. There are different strategies to calculate the autocorrelation functions. In this work, we tested two of them: the classical cross-correlation geometrical normalized (CCGN) and the PCC. The main concept of both approaches are briefly introduced in the following.

Autocorrelations are computed in full analogy to the cross correlations and measure the similarity of a seismic trace with a delayed version of itself. In the case of CCGN, the classical correlation is normalized by the energy within the considered time windows to limit the correlation values between −1 and 1. It further decreases the sensitivity of the correlation to amplitude changes in the data. Still, CCGN is biased by energetic signals such as those caused by earthquakes, instrument failure, local noise, and so on (Schimmel et al., 2011). This sort of bias is usually attenuated by also normalizing the data during the preprocessing (e.g., Bensen et al., 2007). These normalizations basically consist in balancing the amplitudes in the time and frequency domain.

The PCC does not involve signal amplitudes since it is solely based on the similarity of the instantaneous phases obtained through analytical signal theory, which allows one to split any real-valued time series into an instantaneous amplitude and phase function. The instantaneous phases are the same for exactly similar waveforms independent of their amplitudes, and their closeness is used to measure waveform similarity. For further details on the PCC and CCGN, please see supporting information section S1.

Autocorrelation functions are usually stacked until a robust structure response is found. Incoherent signals or noise are attenuated during the stacking process while stationary signals are build up. Different stacking techniques can be employed. The linear stack, a simple sum normalized by the number of stacked records, is commonly used. Here we employed the time-frequency domain phase weighted stack (tf-PWS), introduced by Schimmel and Gallart (2007). tf-PWS is the linear stack weighted by the time-frequency-dependent instantaneous phase coherency to enhance coherent signals independent of their amplitudes. Coherent signal enhancement is achieved through attenuating incoherent signals. tf-PWS is the time-frequency domain extension of the phase-weighted stack presented by Schimmel and Paulssen (1997). For further details, please see Schimmel et al. (2011). Both, PCC and tf-PWS, have already been used with ambient noise data (D'Hour et al., 2016; Haned et al., 2016; Taylor et al., 2016, among others).

In the following sections, we describe the processing sequence adopted in our study and the assumptions and conclusions obtained from several tests to finally present and interpret our results, a map of the crystalline basement of the Ebro Basin.

2. Data and Processing

We processed data from 42 stations located sparsely along the Ebro Basin (Figure 1). Four of the stations are permanent and belong to the National Geographic Institute of Spain. All the other stations were operational during different data acquisition campaigns of the Institute of Earth Science Jaume Almera. Eight stations were deployed specially for this study in the central area of the basin. The operation time of these stations varies from 3 months to a couple of years between 2011 and 2016. Although the stations are from different surveys there is a high homogeneity in the recording parameters. All stations are three-component broadband with sampling rate of 100 Hz.

Although there are dozens of wells drilled in the Ebro Basin, only 29 wells reached the Paleozoic basement and are used in this work to identify and/or validate the reflections retrieved with the autocorrelations. Further, we used information of lithology (Lanaja, 1987) to aid our interpretation and from sonic logs to build seismic velocity models (Choukroune et al., 1990; Gil & Jurado, 1998; ITGE, 1990; Julià et al., 1998; Jurado, 1989; Pedreira, 2005) for the reflector depth estimation.

We used vertical component data, where most of the reflected *P* wave energy is expected to be recorded, cut into nonoverlapping 1-hr segments and zero-phase band-pass filtered. Different frequency bands were

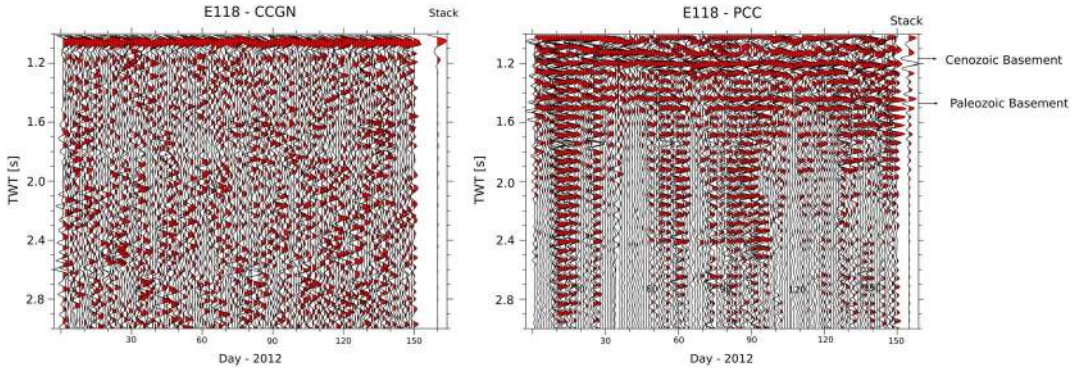

Figure 2. Section plot of daily autocorrelation functions computed with cross-correlation geometrical normalized (CCGN; left) and phase cross correlation (PCC; right). The trace to the right of each panel is the total autocorrelogram stack. All stacks were calculated with time-frequency domain phase weighted stack. TWT = two-way time.

tested. The shallower the subsurface targets are, the higher the frequency band must be to resolve the reflectors and to avoid the interference of the *P* wave reflection with sidelobes of the zero-lag autocorrelation peak. Lower and upper corner frequencies are ranging between 3–4 Hz and 9–18 Hz, respectively. For CCGN, the data were normalized in the time and frequency domain (1-bit normalization and spectral whitening) to avoid contamination and bias from high-amplitude signals (Bensen et al., 2007). For PCC the data were only band passed since outlying amplitude events do not affect the PCC results (Schimmel et al., 2011). The autocorrelations were computed for each 1-hr segment with maximum time lag up to 10 s and stacked to generate daily autocorrelation functions. The daily autocorrelation functions are used to identify time variability as might be caused by varying weather or other noise source conditions and to assess the robustness of the reflection response. Further, all the individual autocorrelations were stacked to obtain one total autocorrelation stack per station used for final interpretation and further analysis. For example, all travel time measurements were taken on the total autocorrelations stacks. The total amount of processed data per station ranges from 30 days to 2 years.

Figure 2 shows the daily autocorrelation functions (CCGN and PCC) for station E118 located in the central part of the basin. The stack of all available autocorrelograms is shown to the right of each panel. The daily CCGN autocorrelagrams show a high waveform variability, that is, no stable structural response or signal can be identified. On the contrary, the daily PCC autocorrelograms show signals that are repeated day by day and interpreted as part of the reflection response. The structural response is enhanced for some subsequent days, likely due to varying meteorological conditions. In Figure 2 the marked reflectors have been identified with the support of well data as explained in sections 3.1 and 3.2. For all our stations clearer reflections are found using PCC. The preprocessing applied to the CCGN data alters the waveforms that hampers building up a stable reflection response. CCGN without preprocessing is, however, inadvisable due to the recorded seismicity of the Pyrenees. Besides, body wave reflections are expected to have low amplitudes in the ambient noise (e.g., Draganov et al., 2009; Roux et al., 2005) and are therefore likely better detected by their phase coherence, that is, by an amplitude unbiased approach. For this reason, and after several tests, PCC was chosen as the correlation approach for the continuation of this study.

We also computed autocorrelations for lower frequencies (2–4 Hz) and up to 20-s lag time to test our approach through detecting other reflections such as the Moho and intracrustal discontinuities. For example, the Moho is well detected and two examples are shown in the supporting information section (Figure S1).

3. Application to Field Data

3.1. General Aspects of Autocorrelations for the Ebro Basin

Figure 3 shows an example of a daily section plot for station CE03 along with its geological interpretation. The geological meaning of the identified reflectors were determined with the support of the lithological data from wells drilled around the station location. Synthetic tests based on well data are presented in the next section. This station is located in the Sub-Pyrenees basin, a complex zone with thrusts and folds related to the Pyrenees thrust system (see Figure S2 for the exact station location). We identified an intermediate reflection coming

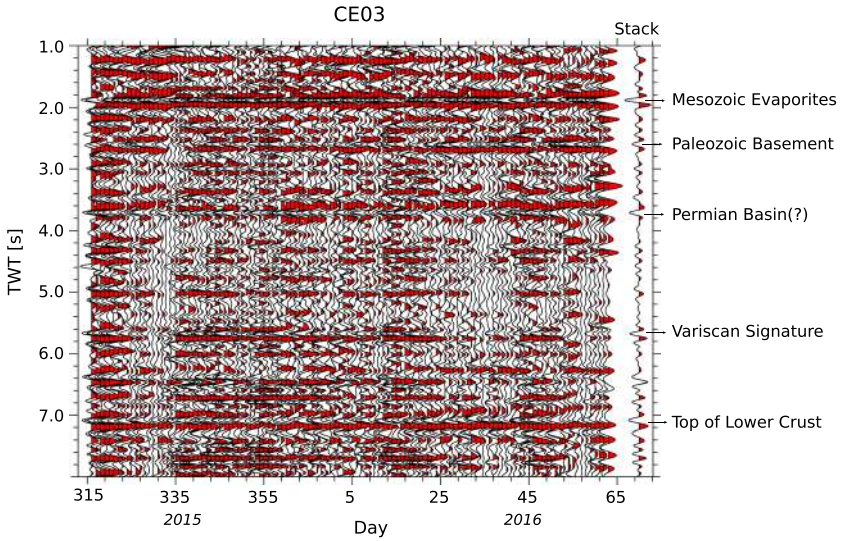

Figure 3. Daily autocorrelation section for station CE03 with the corresponding total autocorrelagram stack to the right and interpretation based on adjacent well data. The correlations were computed using phase cross correlation on 3- to 12-Hz band-pass filtered data and stacked using time-frequency domain phase weighted stack. Positive amplitudes are in red. Polarity has not been changed and a negative polarity indicates a positive impedance contrast. TWT = two-way time.

from a high contrast layer above the basement at 1.9-s two-way time (TWT) inferred as evaporites from the Cenozoic. The basement *P* wave arrival (2.6 s) is followed by a low-reflectivity pattern, also observed for several other stations. The lower amplitude of the basement reflection may be due to the lack of energy trapped in more superficial layers, or by the fact that the impedance contrast is smaller, or by a decreased detectability due to scattering. The average seismic velocity for this zone, extracted from well logs (ITGE, 1990), changes from 3.8 km/s in Cenozoic sediments to 5.2 km/s in the Mesozoic sediments. The velocity of the Paleozoic basement is 6 km/s in the Ebro Basin (Banda, 1996). The data from Figure 3 show another strong reflection at 3.7 s. Choukroune et al. (1990) raised the possibility of this reflector being a signature of a Permian Basin. Reflections between 2.5 (south area) and 4 s TWT (north area) are detected for all stations; however, their geological meaning is not clear yet. The arrival at 5.6 s TWT is the seismic signature of the Variscan structure. Choukroune et al. (1990) first identified this reflection pattern during the Etude de la croûte Continentale et Océanique par Réflexion et Réfraction Sismiques (ECORS) project and interpreted this as an imbricated thrust system. This reflector is seen for all stations in the north of the study area. For stations to the south, its identification is not always possible due to the use of higher-frequency bands. At 7.1 s, a strong reflection is detected and associated to the top of the deep crust, what is recognized to be at about 21-km depth below the Ebro Basin (Banda, 1996).

3.2. EGF Retrieval and Numerical Tests

We computed the Green's function and the correspondent noise autocorrelogram for a single one-layer model using the finite difference (FD) algorithm from Thorbecke and Draganov (2011). The superior layer has a thickness of 2.5 km and velocity of 5 km/s. The velocity of the half-space is 6 km/s as found in the crystalline basement of the Ebro Basin. For the particle velocity Green's function computation, an impulse source with a Ricker wavelet of peak frequency of 15 Hz was used. The single vertical component velocity receiver has been positioned at the point source (at 25 km in Figure 4) to obtain the zero-offset reflection response shown as the solid green line in Figure 4. For the autocorrelation, noise sources are positioned randomly in the subsurface between 4 and 6 km depth with random source signatures but limited frequency content comparable to the real data (up to 20 Hz). We used 8,000 random sources within a 10-s time window recorded at 500 different station positions to obtain 500 time series for the autocorrelations of the same 1-D model. The computed time series are submitted to the same processing sequence as the field data, and the autocorrelations are stacked to produce the final trace, which is shown with a dashed red line in Figure 4.

The comparison of the noise autocorrelation with the velocity Green's Function shows that both are similar and that the *P* wave reflection at the increased impedance contrast causes a negative amplitude signal. This

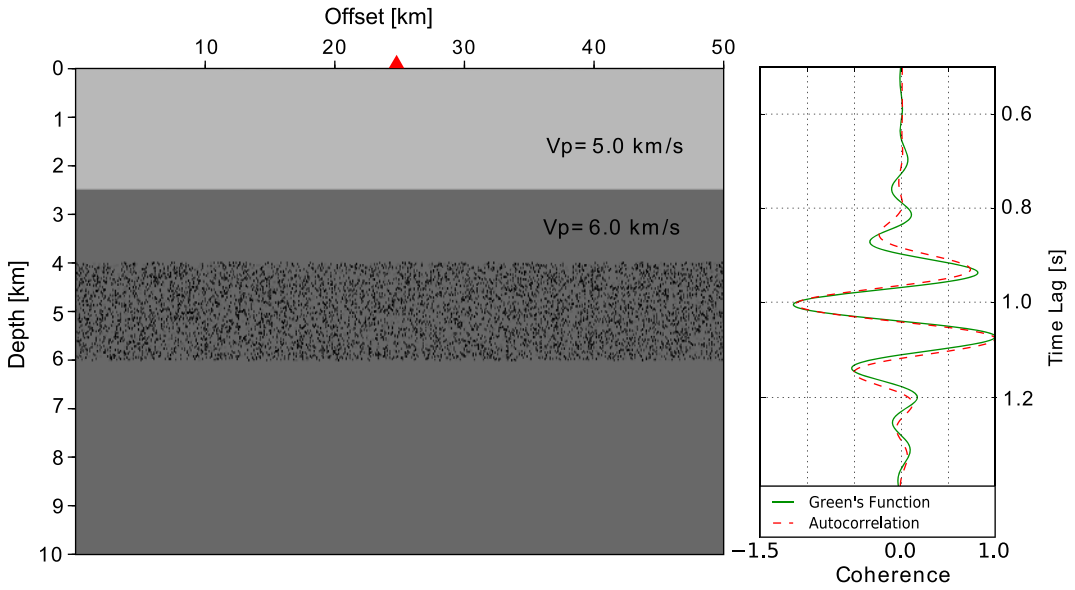

Figure 4. Green's function and autocorrelation function for a simple model (left). Red triangle marks the source and receiver location for the Green's Function computation. Black dots at 4- to 6-km depth are the random sources for the noise simulation. The autocorrelation (dashed red line) of the simulated noise data and Green's function (green line) are shown in the right panel.

numerical test supports our processing as the data were recorded at broadband seismometers which work as velocity transducers within a wide frequency band. The instrument response was not removed from the data. The frequency band used in our analysis is in the flat plateau of the sensor response meaning that the seismic recordings are proportional to ground velocity. The autocorrelation of the velocity recordings is, therefore, proportional to the EGF for particle velocity (Sabra, 2005). We do not change the polarity of the autocorrelations, and hence, the time picking and interpretation was made following the (usually) strongest negative peak in the total autocorrelation stack.

To understand the autocorrelations under the specific geological conditions, we generated synthetic data for stations CE03 and CE04 using available well logs to build a velocity model and the FD model package from Thorbecke and Draganov (2011). The station and well positions are highlighted in Figures 8 (small black boxes) and S2. For station CE03, we used the lithological information from well P460 (Surpirinaica-1), 15 km away from CE03. For station CE04, we used well P121 (Ejea-1), which is located at 7-km distance from the station. The velocity models were extracted from the corresponding well logs (ITGE, 1990; Lanaja, 1987) and simplified for the subsequent synthetic test computation. The synthetic data was processed using the same work flow as with the field data. All autocorrelations were calculated with PCC.

The model for station CE03 (Figure 5a) shows that the first reflection seen at 1.8-s TWT is due to the evaporite bed found in the Mesozoic sequence, while the Paleozoic basement reflection is detected with slightly smaller amplitude at 2.6-s TWT. The difference in time for the first reflection (about 0.2-s TWT) is explained by the distance to the well and different shallow structure at the station due to its proximity to the fold and thrust front of the Pyrenees. At 3.7 s appears a multiple reflection from the first layer as seen in the synthetic data and which also coincides with a signal in the field data autocorrelogram. However, as discussed earlier, reflections from a possible Permian Basin or due to reworked sediments from the Pyrenees thrust system are also expected to occur at similar TWT.

For CE04, we built an 1-D geological model that comprises a Cenozoic salt bed at 2-km depth, the Cenozoic basement at 2.7-km, and the Paleozoic basement at 3-km depth. The corresponding synthetic autocorrelation for station CE04 is quite complex due to the added shallow layer but very similar to the field data (Figure 5b). It is seen that the Cenozoic basement is totally masked by the shallower reflections related to the fast evaporites layer; nevertheless, the Paleozoic basement is clearly detected at 1.5-s TWT.

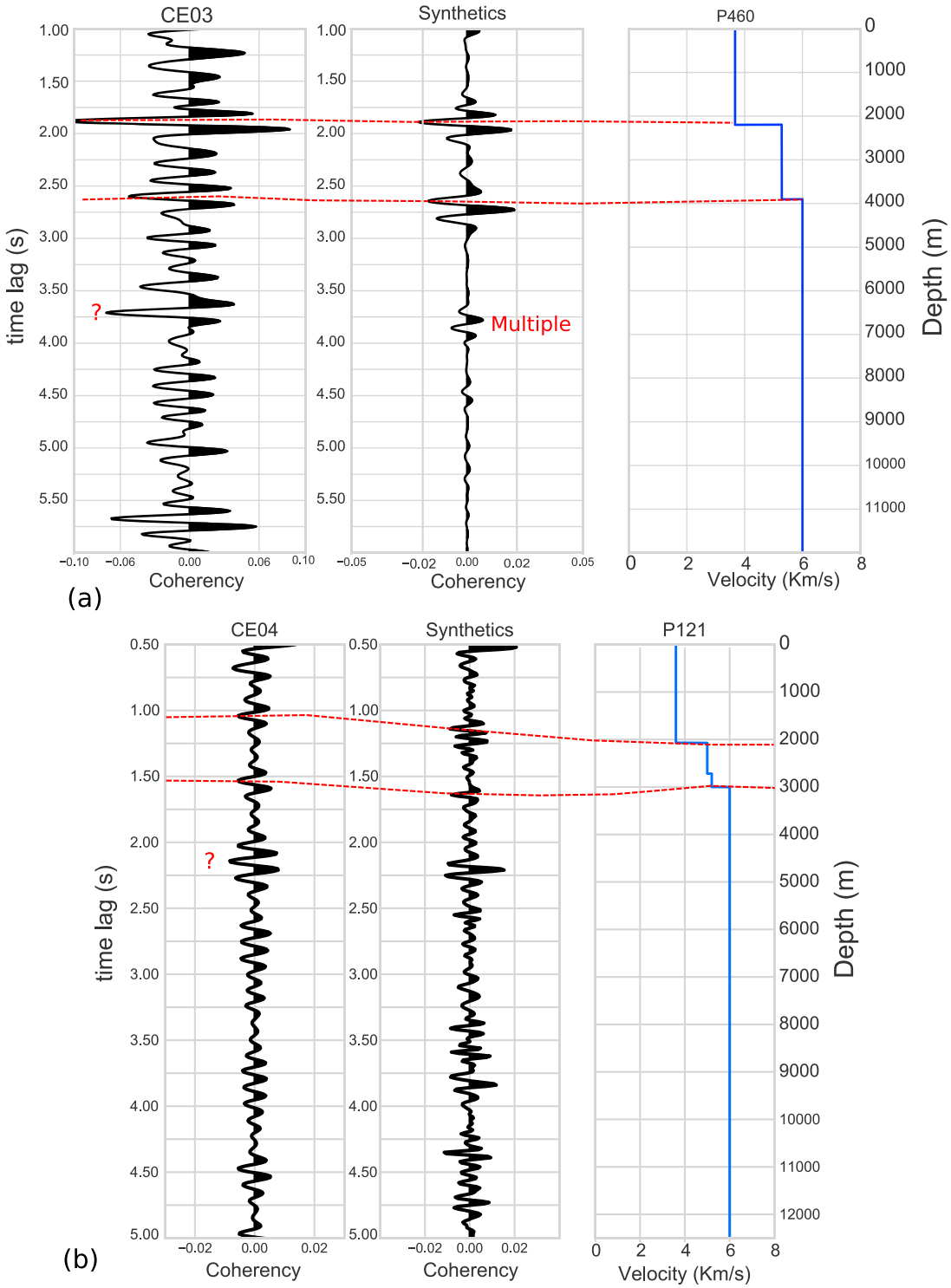

Figure 5. Comparison of autocorrelations computed for field data and synthetic data for station CE03 (a) and CE04 (b). The synthetics were computed for simplified velocity models (rightmost panels) based on adjacent wells P460 and P121, respectively.

3.3. Frequency Stability and Autocorrelation Sidelobes

A challenge faced during the interpretation of the field data are sidelobes which may mask early *P* wave arrivals. The sidelobes are caused by the convolution of a delta pulse at zero time lag with the effective noise source time function (e.g., Ruigrok & Wapenaar, 2012). In the following, we may refer to them as zero-lag sidelobes. Shallow reflectors produce signals with short TWT, which may interfere with the zero-lag sidelobes

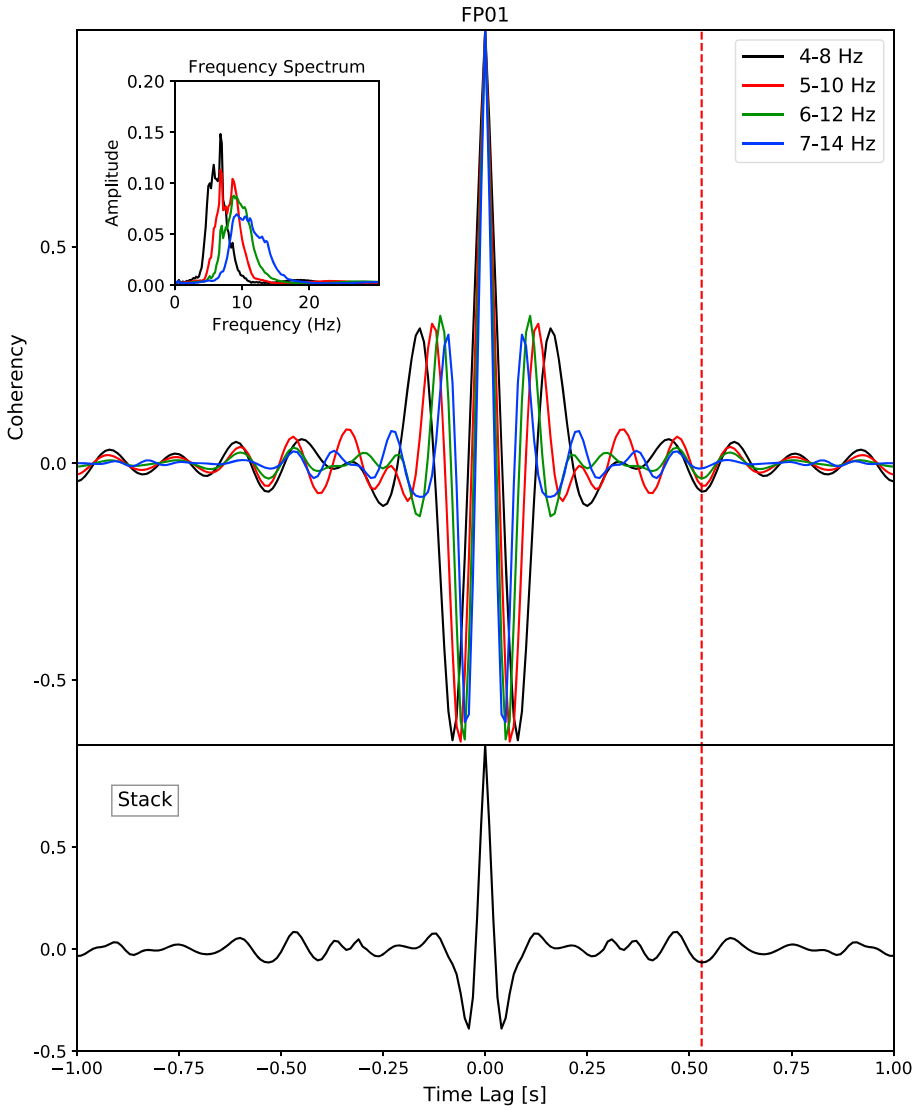

Figure 6. (top) Autocorrelation functions for station FP01 as function of frequency band. The dashed red line marks the consistent *P* wave reflection. Note the variability of the frequency-dependent zero-lag sidelobes. (bottom) Stack of all autocorrelations shown to the top. The stack attenuates the sidelobes, while the reflection signal remains clearly visible.

to produce biased or false arrivals. The sidelobes intensity and wavelength are highly dependent of the frequency bandwidth of the autocorrelation function, while a proper *P* wave reflection should stay more stable. This has been tested and is being used to discern shallow *P* wave reflections as shown in Figure 6. The top panel shows the total autocorrelation stack for station FP01 for different one-octave frequency bands. It can be seen from this figure that the sidelobes clearly differ for different frequencies, while the negative peak of the reflection at about 0.55-s TWT stays stable for all frequencies. Further, for higher-frequency bands the reflection pulse is more distant from the sidelobes. The bottom panel shows the stacked autocorrelograms. The sidelobes are attenuated as expected for differing signals; however, the 0.55-s peak is enhanced confirming a consistent reflection seen with varying frequency bands. We basically use this strategy for identification purposes, whenever there may exist ambiguities, that is, mostly for the shallower reflectors. The final data processing is then performed in a frequency band that permits to observe the reflections without visible interference of sidelobes. Alternatively, one may also use these stacks (Figure 6, bottom panel).

3.4. Time Stability

The *P* wave reflection of the basement should be a stable arrival detected throughout the entire operation time of a station. Signal variability or absence during determined periods of time may indicate that the signal is

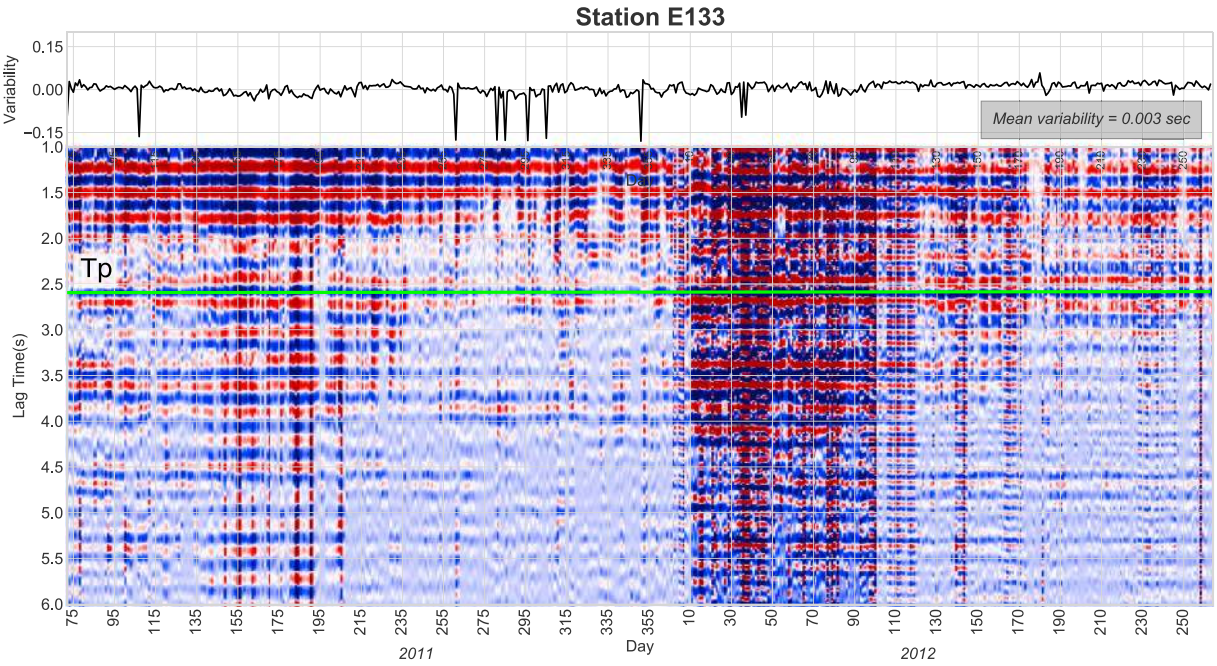

Figure 7. (bottom) Daily autocorrelagram section for 2 years of data recorded at Station E133. (top) Arrival time differences between the *P* wave reflection measured at about 2.6-s TWT on daily autocorrelograms and the same arrival in the total autocorrelogram stack for all data. Blue indicates negative polarity and red positive polarity.

due to the occurrence of punctual ambient or cultural noise. For example, noise sources that are not homogeneously distributed may cause a displaced arrival time or even spurious signals (Thorbecke & Draganov, 2011). To assess the variability and precision of the measured reflection time, we calculated the differences between the reflection peak of each daily autocorrelogram and the reference trace obtained stacking the autocorrelations for 2 years of data recorded at station E133 located in the Sub-Pyrenees basin (Figure S2). Before comparison, the data were resampled to 200 Hz to increase temporal resolution. Figure 7 shows a section of the daily autocorrelation functions (bottom) and the measured time variation of the negative reflection peak between the daily autocorrelograms and the total autocorrelagram stack (top).

The variation in the *P* wave arrival time is very small and not related with systematic seasonal variations of the noise wave field, although the amplitude of the waveform becomes weaker between days 260 and 320 of year 2011. During this period, the time variability is slightly increased, which is probably due to a small number of active sources or due to weak sources possibly accompanied by a different source distribution.

From this analysis, the average time difference between individual days and the reference trace is 3 ms, which is equivalent to a reflector displacement of about 15 m. This illustrates the robustness of our results toward the variability of the ambient noise wave field as consequence of source changeability due to varying meteorological phenomena or anthropogenic activity.

3.5. Basement Map Construction

We processed the noise recordings of 42 stations using the procedure described before. For 37 stations, robust *P* wave reflections could be detected as isolated and clear signals. Only for five stations, no consistent reflection responses were obtained for the target frequency band. This is likely attributed to the lack of energy in the noise wave field, the presence of other coherent noise sources close to the station (such as pumps in operation), and/or structural complexities, which inhibit a comprehensible reflection response. The final geological interpretation of the autocorrelograms was made using the available well log data from the neighborhood of each station. The measured TWT for the Paleozoic basement reflections are shown in Figure S3. For the time-to-depth conversion of the measured arrivals, we divided the basin into three regions ((1) the central Ebro Basin, (2) the Sub-Pyrenees Basin, and (3) the east Ebro Basin — Figure S3) to account for lateral heterogeneity in the basin. The subsurface velocities were derived both from available well logs and from active seismic experiments (Choukroune et al., 1990; Gil & Jurado, 1998; ITGE, 1990; Julià et al., 1998;

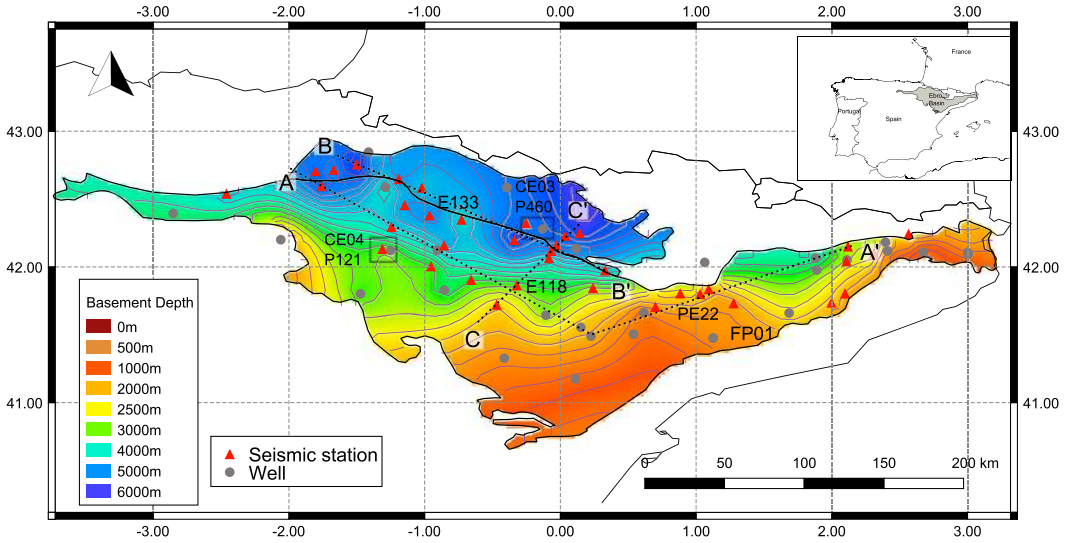

Figure 8. Final Map of the Paleozoic basement depth. Dashed black lines indicate the profiles presented in Figure 9. The two small black boxes mark stations CE03, CE04, and corresponding wells used for Figure 5.

Jurado, 1989; Pedreira, 2005). For the central Ebro Basin, we used *P* wave velocities of 3.6 and 5.1 km/s for Cenozoic and Mesozoic sediments, respectively. For stations in the Sub-Pyrenees Basin we assume a velocity of 3.8 km/s for Cenozoic and 5.2 km/s for Mesozoic, while for the stations located in the east Ebro Basin a constant velocity of 5.1 km/s is applied in the conversion.

The depth values for the Paleozoic Ebro Basin, obtained from 37 stations have been contoured together with depth measurements from 29 wells that reached the Paleozoic basement and are shown in Figure 8. The measured reflection times and converted depth values are also listed in Table S1 of the supporting information section. Figure 8 shows a clear north-south trend of decreasing depth values as it is expected from the TWT measurements (Figure S3). The exact depth values, nevertheless, may vary as function of the employed velocity model. If the time-to-depth conversion is performed with an average constant velocity of 4.5 km/s, then the basement depths increase on average about 160 m. For a constant velocity of 5 km/s, this average increases to 247 m. The depth variations are larger for stations in the north, the deepest portion of the basin.

4. Final Basement Map

The Paleozoic basement topography (Figure 8) shows a main dip to the north/northwest toward the Pyrenees. In contrast to the top of the Cenozoic basement (Gaspar et al., 2001), our Paleozoic basement map does not show a very complex structure. Nonetheless, a larger depth variation is observed closer to the Pyrenees thrust front, likely due to the increased geological complexity. There is a lack of seismic data in the south of the basin, but wells fill this gap and provide enough information to map the basement behavior. The deeper areas of the basin are close to the Pyrenees due to the flexural history related to the mountain origin (Gaspar et al., 2001). A thick sedimentary cover is also observed to the west. This feature is only constrained by one station and two wells and likely related to the high subsidence of this area of the basin, probably due to the thrust system not only from Pyrenees but also the Cantabric Ridge (Pedreira, 2005; Riba & Jurado, 1992). The sedimentary thickness of the central Ebro Basin varies from 700 to 2,500 m, in the westernmost part from 2,000 to 5,000 m and in the sub-Pyrenees zone from 4,000 to 6,000 m. The east extreme also shows a different trend in Paleozoic basement depth because it suffered uplift and erosion during the opening of the Valencia Through.

From the basement map, three depth profiles were built to show the similarities and differences between the total autocorrelation stacks, as well as the lateral continuity of the basement structure (Figure 9). A time-dependent amplitude gain of $t^{0.8}$ was applied to each normalized trace to improve the visual inspection of later arrivals through more balanced amplitudes. Profile A-A′ crosses the basin from west to east. It is visible that the autocorrelograms can be related to the well data. A high lateral coherence of the reflection response is, however, not observed probably due to structural variability, superficial layers, and other

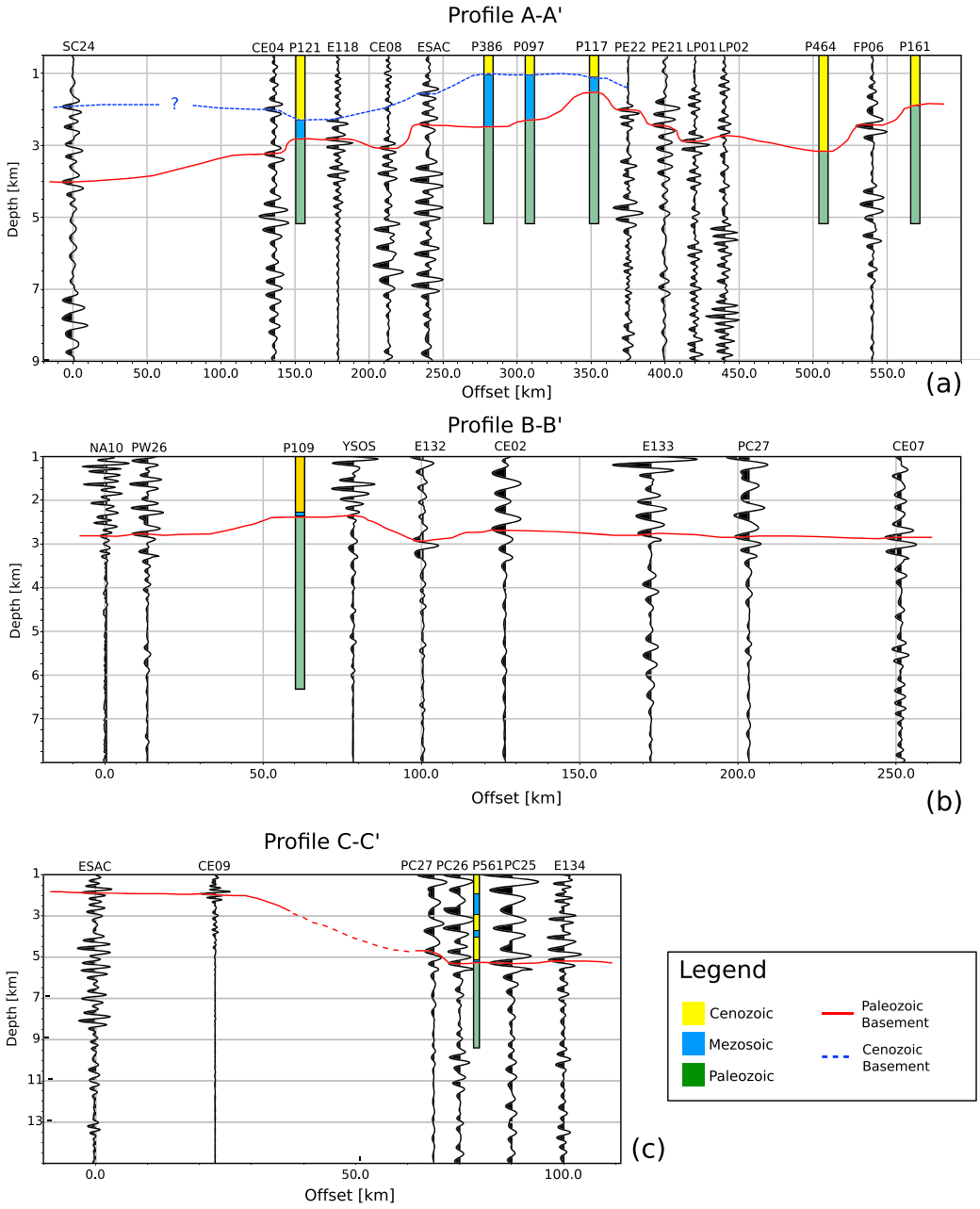

Figure 9. Three profiles built with well data and autocorrelation functions. Profile locations are shown in Figure 8. Amplitudes of autocorrelations were balanced by a factor of $t^{0.8}$ to increase the visibility of later arrivals. Red line shows the Paleozoic basement topography and blue line the possible Cenozoic basement only seen in Profile A-A′. Different frequency bands and geological complexity cause the variable reflection response along the profiles.

small-scale geological complexity. A substantial variation of the reflectivity has also been reported by Kennett et al. (2015), who employed spatial stacks of neighboring stations to improve lateral coherence and to aid the signal detection. Here we performed no lateral smoothing and based the *P* wave detections on the daily autocorrelogram sections (e.g., Figures 2 and 3) and well data. Two examples of daily autocorrelation section for stations SC24 and PE21 from profile A-A′ are shown in the supporting information section (Figures S4 and S5) to highlight the robustness and visibility of the interpreted signals. The difference between the autocorrelograms of Figure 9 is caused also by the different frequency bands to adapt to the geological structure and noise wave field at each station. Stations located in areas with shallower basement demand higher-frequency filters to resolve shallower reflectors and to avoid the signal to be contaminated by the zero-lag sidelobes of

the autocorrelations. One may try to balance the frequency contents in an added postprocessing step which, however, we did not do to stay with the minimum processing required to obtain results and to avoid masking the real procedure and data.

The second profile B-B′ is located in a zone with deeper basement and more complex geology, although the basement depth itself is varying smoothly between 4 and 5 km. The autocorrelations look more similar because there is less variation in the dominant frequency band.

The different autocorrelogram appearance inherent to the varying frequency bands used is also evident in the S-N profile (C-C′). The well P561, in this profile, further highlights the complexity of the geology in the area with thrusts and folds. The well cuts twice the Cenozoic-Mesozoic sequence (yellow and blue, respectively) before reaching the Paleozoic basement at 5,000-m depth. This complexity causes strong ripples close to the basement reflection time as seen in the stations autocorrelograms.

5. Discussion

With the approach presented in this work, we obtained 37 new high-resolution depth measurements of the Paleozoic basement in the Ebro Basin. These measurements fill in holes in the basement coverage based on 29 wells and made it possible to present a more accurate basement map. A total of 42 stations was processed, but 5 of them did not provide unambiguous results and have not been used to extract *P* wave reflections. This might be due to the lack of energy in the target frequency band, the presence of other coherent noise that masks the subsurface reflections (e.g., a pump in operation), the local structural complexity, and/or the presence of a large transitional zone between the sedimentary bed and basement that fades the reflection (Kennett et al., 2015).

We noted in our analysis that the total operation length of a station is not crucial for the analysis as also observed by Gorbatov et al. (2013). In fact, a stable reflection response can be retrieved using few days of data. For station CE07, only 30 days of continuous data were acquired and processed delivering confident results. Nevertheless, being able to use long daily autocorrelogram sections provides more confidence in the interpretation since it allows one to assess the stability of the reflections with respect to wave field variability caused by changes in meteorological conditions or the influence of anthropogenic noise sources. In our analysis of section 3.4 we determined an average daily TWT variation of 3 ms, which translates to a discontinuity change of about 15 m (about 2–3% of the reflector depth). Nonetheless, our measurements are based on the total autocorrelation stacks of several weeks to a couple of years, which reduces through averaging any arrival time variability. Larger errors are expected from the time-to-depth conversions through inaccurate velocity models. Our models are based on well data and active source surveys (Choukroune et al., 1990; Gil & Jurado, 1998; ITGE, 1990; Julià et al., 1998; Jurado, 1989; Pedreira, 2005). Depth errors due to inaccurate velocity models would be systematic but are not expected to be larger than 100 or 200 m. We therefore also provide our TWT measurements that are free of any velocity model.

In this study we could not find a fixed frequency band to perform an automated autocorrelation study, but we found that a 3- to 12-Hz band-pass filter is often suited to obtain good reflection responses for most of the stations. Those stations located in the shallower part, however, required a higher-frequency band to detect clear body wave reflections with high signal to noise ratio and with no contamination of the zero-lag sidelobes of the autocorrelation functions. The sidelobes may interfere with the shallow reflection response. This can be controlled using different frequency bands since the reflection arrival time is expected to vary less than the frequency-dependent sidelobe position.

The accurate picking of the *P* wave arrival must be done carefully. Gorbatov et al. (2013) have chosen to pick the latest (deepest) arrival as the Moho *P* wave reflection. Kennett et al. (2015) used, for some of their autocorrelation functions, the change in the reflectivity patterns to detect the correct arrival time. In this work we picked the strongest reflection whenever it is followed by a change in reflectivity in the following milliseconds, but not necessary immediately after the reflection to account for the ringing effect caused by the presence of shallow layers that can affect some stations (e.g., CE04). Further, the section plot of daily autocorrelograms proved to be useful for the signal identification as it helped to reduce ambiguities and to discover features that are not consistent in time.

The complexity of the reflection response is related to the subsurface heterogeneities, and a simple identifiable *P* wave reflection at the basement is only expected for those stations where the target discontinuity is sharp enough. With the support of the a priori knowledge from well information we identified and extracted

reflections, even when the subsurface geology is complex such as in the Jaca Basin (e.g., station CE03, Figure 3). A variable reflectivity of the basement and the presence of other volumetric heterogeneities can explain the low lateral coherence of the reflection response obtained for stations separated by about 10–50 km as seen in the profiles presented in Figure 9. A denser station deployment is expected to provide a more similar reflection response for neighboring stations, which would permit to better track any reflector. It would also allow one to apply the lateral averaging proposed by Kennett et al. (2015) without averaging over too long of a distance range. At some stations double (or triple) reflections can be observed, which can be due to shallow layering or a transition zone at the Paleozoic basement (Gorbatov et al., 2013).

Although the Cenozoic sequence of the Ebro basin is target of different studies and new data have being published, the Paleozoic basement of the Ebro Basin is still based on geophysical data from the 1990s and older (IGME, 2009; ITGE, 1990). The updated map presented in IGME (2009) adds to ITGE (1990) new information from geological cross sections at the edges of the basin and decreased ambiguities in the Pyrenees thrust front where the seismic data quality was low. The identification and mapping of the deep horizons using the available seismic images is often difficult due to the presence of evaporite layers and due to the acquisition design caused by complex topography in the pre-Pyrenees and Pyrenees (ITGE, 1990) which inhibits a linear station deployment aligned with an active source. Using a single station approach as presented here does avoid these difficulties and therefore provide new valuable measurements. The evaporites beds also affected the autocorrelations, nevertheless, PCC permitted us to detect the coherent weak-amplitude subsalt reflections from the Paleozoic basement. Our map shows the same overall structure with the basement dipping toward the Cantabrian (westward) and Pyrenees (northward) mountain ranges. The Paleozoic isobaths map from IGME (2009) further shows the Paleozoic raising up below the Pyrenees until it outcrops in the axial zone of the mountain range.

The geological complexity of the north basin margin caused by the thrust system of the Pyrenees (e.g., Verges et al., 2002) and autochthonous basement blocks is less evident in our map since we are using only direct measurements (well data and ambient noise autocorrelations). In the east part of the basin, our results show a slightly deeper basement in comparison with IGME (2009). It is possible that we overestimated the velocity for the time-to-depth conversion since the Mesozoic sequence (with higher *P* wave velocity) was eroded in some extent of this area (Lanaja, 1987). The interface between the Mesozoic sediments and the Paleozoic basement is difficult to identify in some well logs due to the high deformation suffered by the first (ITGE, 1990), which may have led to some bias.

6. Conclusion

The methodology applied in this study proved to be useful and efficient to map the Paleozoic basement reflector in the Ebro Basin. The Cenozoic basement is, however, hard to delineate due to the presence of salt beds and the Mesozoic sequence, which produces *P* wave signals that cannot be differentiated from the expected Cenozoic basement reflections. Individual autocorrelation functions can be difficult to interpret but in conjunction with well data, ambiguities are reduced and the reflection responses become useful to map shallow subsurface discontinuities. The inspection of daily autocorrelagram sections enables to assess time variability and to find the reflections as consistent signals. Also, the usage of different frequencies is recommended to notice and avoid possible bias from zero-lag sidelobes. This work also benefited from the usage of PCC, since it does not require to attenuate outlying signals as caused by local seismicity, while detecting the weak-amplitude reflections through their phase coherence. In fact, our examples show that PCC was superior to CCGN, which needs more data to find a stable reflection response.

Altogether, ambient noise autocorrelations can be employed as an inexpensive approach to increase the number of depth measurements to yield higher-resolution maps. The most challenging step of the strategy is to eliminate possible ambiguities caused by structural complexity. A denser station deployment and a priori information (e.g., well logs) are therefore very useful to aid in the mapping. The *P* wave reflection identification is expected to be easier in extensional basins with less degree of complexity and higher impedance contrasts.

Most of the recent studies in the Ebro Basin are still based on the Paleozoic map presented by ITGE (1990) and updated by geological surface measurements (IGME, 2009). The new Paleozoic basement map may help to obtain more accurate hypocenter maps and should be useful for 3-D ground amplification and basin (and surrounding range) evolution studies. Our measurements confirm a basin dipping to the north with depocenter toward the Central Pyrenees and Cantabrian Range where the basement depth is about twice as deep as in the east of the basin.

Acknowledgments
We are very thankful to Martha Savage for all work involved with handling the manuscript and to Robert Nowack and Elmer Ruigrok for their careful and constructive reviews. We are very grateful to Mario Ruiz Fernandez for fieldwork, data acquisition, and help with any data problem. This work is funded by the Spanish Project Misterios CGL2013-48601-C2-1-R. We also acknowledge support and discussion through TIDES COST Action ES1401. We are further grateful to J. Thorbecke and D. Draganov for discussion and hosting PR during a 1-week STSM (TIDES) stay at Delft University of Technology. The seismic data belong to the MISTERIOS project and can be accessed at http://geodb.ictja.csic.es/Misterios_CE_HHZ_2015-16. The final basement depth model and correlations/stacking codes are freely distributed by the authors and can also be downloaded from http://diapiro.ictja.csic.es/gt/mschi/SCIENCE/tseries.html#software.

References

Arche, A., & López-Gómez, J. (1996). Origin of the Permian-Triassic Iberian Basin, central-eastern Spain. *Tectonophysics*, *266*(1–4), 443–464. https://doi.org/10.1016/S0040-1951(96)00202-8

Banda, E. (1996). Deep crustal expression of Tertiary basins in Spain. In P. F. Friend & C. J. Dabrio (Eds.), *Tertiary basins of Spain the stratigraphic record of crustal kinematics* (pp. 15–19). Cambridge: Cambridge University Press. https://doi.org/10.1017/CBO9780511524851.007

Bensen, G. D., Ritzwoller, M. H., Barmin, M. P., Levshin, A. L., Lin, F., Moschetti, M. P., et al. (2007). Processing seismic ambient noise data to obtain reliable broad-band surface wave dispersion measurements. *Geophysical Journal International*, *169*(3), 1239–1260. https://doi.org/10.1111/j.1365-246X.2007.03374.x

Choukroune, P., Roure, F., Pinet, B., & Ecors Pyrenees Team (1990). Main results of the ECORS Pyrenees profile. *Tectonophysics*, *173*(1–4), 411–423. https://doi.org/10.1016/0040-1951(90)90234-Y

Claerbout, J. F. (1968). Synthesis of a layered medium from its acoustic transmission response. *Geophysics*, *33*(2), 264–269. https://doi.org/10.1190/1.1439927

D'Hour, V., Schimmel, M., Do Nascimento, A. F., Ferreira, J. M., & Lima Neto, H. C. (2016). Detection of subtle hydromechanical medium changes caused by a small-magnitude earthquake swarm in NE Brazil. *Pure and Applied Geophysics*, *173*(4), 1097–1113. https://doi.org/10.1007/s00024-015-1156-0

Draganov, D., Campman, X., Thorbecke, J., Verdel, A., & Wapenaar, K. (2009). Reflection images from ambient seismic noise. *Geophysics*, *74*(5), A63–A67. https://doi.org/10.1190/1.3193529

Feng, L., & Ritzwoller, M. H. (2017). The effect of sedimentary basins on surface waves that pass through them. *Geophysical Journal International*, *211*(1), 572–592. https://doi.org/10.1093/gji/ggx313

Galetti, E., & Curtis, A. (2012). Generalised receiver functions and seismic interferometry. https://doi.org/10.1016/j.tecto.2011.12.004

Garcia-Castellanos, D., Vergés, J., Gaspar-Escribano, J., & Cloetingh, S. (2003). Interplay between tectonics, climate, and fluvial transport during the Cenozoic evolution of the Ebro Basin (NE Iberia). *Journal of Geophysical Research*, *108*(B7), 2347. https://doi.org/10.1029/2002JB002073

Gaspar, E. J. M., Van, W. J. D., Ter, V. M., Cloetingh, S., Roca, E., Cabrera, L., et al. (2001). Three-dimensional fluxural modelling of the Ebro Basin (NE Iberia). *Geophysical Journal International*, *145*(2), 349–367.

Gil, J. A., & Jurado, M. J. (1998). Geological interpretation and numerical modelling of salt movement in the Barbastro-Balaguer anticline, southern Pyrenees. *Tectonophysics*, *293*(3-4), 141–155. https://doi.org/10.1016/S0040-1951(98)00097-3

Gil-Zepeda, S. A., Luzón, F., Aguirre, J., Morales, J., Sánchez-Sesma, F. J., & Ortiz-Alemá, C. N. (2002). 3D seismic response of the deep basement structure of the Granada Basin (southern Spain). *Bulletin of the Seismological Society of America*, *92*(6), 2163–2176. https://doi.org/10.1785/0120010262

Gorbatov, A., Saygin, E., & Kennett, B. L. N. (2013). Crustal properties from seismic station autocorrelograms. *Geophysical Journal International*, *192*, 861–870. https://doi.org/10.1093/gji/ggs064

Haned, A., Stutzmann, E., Schimmel, M., Kiselev, S., Davaille, A., & Yelles-Chaouche, A. (2016). Global tomography using seismic hum. *Geophysical Journal International*, *204*(2), 1222–1236. https://doi.org/10.1093/gji/ggv516

Hogan, P., & Burbank, D. W. (1996). Evolution of the Jaca Piggyback Basin and emergence of external Sierra, Southern Pyrenees. In P. Hogan (Ed.), *Tertiary basins of Spain the stratigraphyc record of crustal kinematics* (pp. 153–160). Cambridge: Cambridge University Press.

IGME (2009). Plan de selección y caracterización de áreas y estrucutras favorables para el almacenamiento geoógico de CO_2 en España, Teh Rep. docs 64.044 to 64.055. Instituto Geológico y Minero de España, Madrid.

ITGE (1990). Documentos sobre la geologia del subsuelo de España. Tomo VI: Ebro-Pirineos. Instituto Geológico y Minero de España, Madrid.

Julià, J., Vila, J., & Macià, R. (1998). The receiver structure beneath the Ebro basin, Iberian Peninsula. *Bulletin of the Seismological Society of America*, *88*(6), 1538–1547.

Jurado, M. (1989). Diagrafías: Su aplicación en el análisis sedimentario. *Revista de la Sociedad de Geólogos de España*, *2*, 291–301.

Kennett, B. L. N., Saygin, E., & Salmon, M. (2015). Stacking autocorrelograms to map Moho depth with high spatial resolution in southeastern Australia. *Geophysical Research Letters*, *42*, 7490–7497. https://doi.org/10.1002/2015GL065345

Lanaja, J. M. (1987). *Contribución de la exploración petrolífera al conocimiento de la geología de España* (1–465 pp.). Instituto Geológico y Minero de España, Madrid.

Langston, C. (1979). Structure under Mount Rainier, Washington, inferred from teleseismic body waves. *Journal of Geophysical Research*, *84*(B9), 4749. https://doi.org/10.1029/JB084iB09p04749

Narayan, J. P., & Singh, P. K. (2016). Kamal Effects of basin parameters on the spatial variation of characteristics of basin generated Rayleigh waves. *International Journal of Geo-Engineering*, *7*(1), 17. https://doi.org/10.1186/s40703-016-0031-x

Oren, C., & Nowack, R. L. (2016). Seismic body-wave interferometry using noise autocorrelations for crustal. *Geophysical Journal International*, *208*, 321–332.

Pedreira, D. (2005). Estructura cortical de la zona de transición entre los Pirineos y la Cordillera Cantábrica (PhD thesis). University of Oviedo. https://doi.org/84-8317-528.2

Riba, O., & Jurado, M. (1992). Reflexiones sobre la geología de la parte occidental de la Depresión del Ebro. *Acta Geologica Hispanica*, *27*(1), 177–193.

Roux, P., Sabra, K. G., Gerstoft, P., Kuperman, W. A., & Fehler, M. C. (2005). *P* waves from cross-correlation of seismic noise. *Geophysical Research Letters*, *32*, L19303. https://doi.org/10.1029/2005GL023803

Ruigrok, E., Campman, X., & Wapenaar, K. (2011). Extraction of P-wave reflections from microseisms. *Comptes Rendus Geoscience*, *343*(8–9), 512–525. https://doi.org/10.1016/J.CRTE.2011.02.006

Ruigrok, E., Campman, X., & Wapenaar, K. (2012). Basin delineation with a 40-hour passive seismic record. *Bulletin of the Seismological Society of America*, *102*(5), 2165–2176. https://doi.org/10.1785/0120110242

Ruigrok, E., & Wapenaar, K. (2012). Global-phase seismic interferometry unveils *P* wave reflectivity below the Himalayas and Tibet. *Geophysical Research Letters*, *39*, L11303. https://doi.org/10.1029/2012GL051672

Sabra, K. G. (2005). Extracting time-domain Green's function estimates from ambient seismic noise. *Geophysical Research Letters*, *32*, L03310. https://doi.org/10.1029/2004GL021862

Saygin, E., Cummins, P. R., & Lumley, D. (2017). Retrieval of the *P* wave reflectivity response from autocorrelation of seismic noise: Jakarta Basin, Indonesia. *Geophysical Research Letters*, *44*, 792–799. https://doi.org/10.1002/2016GL071363

Schimmel, M. (1999). Phase cross-correlations: Design, comparisons, and applications. *Bulletin of the Seismological Society of America*, *89*(5), 1366–1378.

Schimmel, M., & Gallart, J. (2007). Frequency-dependent phase coherence for noise suppression in seismic array data. *Journal of Geophysical Research*, *112*, B04303. https://doi.org/10.1029/2006JB004680

Schimmel, M., & Paulssen, H. (1997). Noise reduction and detection of weak, coherent signals through phase-weighted stacks. *Geophysical Journal International*, *130*(2), 497–505. https://doi.org/10.1111/j.1365-246X.1997. tb05664.x

Schimmel, M., Stutzmann, E., & Gallart, J. (2011). Using instantaneous phase coherence for signal extraction from ambient noise data at a local to a global scale. *Geophysical Journal International*, *184*(1), 494–506. https://doi.org/10.1111/j.1365-246X.2010.04861.x

Taylor, G., Rost, S., & Houseman, G. (2016). Crustal imaging across the North Anatolian Fault Zone from the autocorrelation of ambient seismic noise. *Geophysical Research Letters*, *43*, 2502–2509. https://doi.org/10.1002/2016GL067715

Thorbecke, J., & Draganov, D. (2011). Finite-difference modeling experiments for seismic interferometry. *Geophysics*, *76*(6), H1–H18. https://doi.org/10.1190/geo2010-0039.1

Tibuleac, I. M., & von Seggern, D. (2012). Crust-mantle boundary reflectors in Nevada from ambient seismic noise autocorrelations. *Geophysical Journal International*, *189*, 493–500. https://doi.org/10.1111/j.1365-246X. 2011.05336.x

Verges, J., Fernandez, M., & Martinez, A. (2002). The Pyrenean orogen: Pre-, syn-, and post-collisional evolution. *Journal of the Virtual Explorer*, *8*, 55–74.

Wapenaar, K. (2004). Retrieving the elastodynamic Green's function of an arbitrary inhomogeneous medium by cross correlation. *Physical Review Letters*, *93*(25), 1–4. https://doi.org/10.1103/PhysRevLett.93.254301